Astronomy & Astrophysics

Coronal mass ejection followed by a prominence eruption and a plasma blob as observed by Solar Orbiter[*]

A. Bemporad[1], V. Andretta[2], R. Susino[1], S. Mancuso[1], D. Spadaro[3], M. Mierla[4,5], D. Berghmans[4],
E. D'Huys[4], A. N. Zhukov[4,6], D.-C. Talpeanu[4,7], R. Colaninno[8], P. Hess[8], J. Koza[9], S. Jejčič[10,11], P. Heinzel[12],
E. Antonucci[17], V. Da Deppo[13,17], S. Fineschi[1], F. Frassati[1], G. Jerse[14], F. Landini[1], G. Naletto[15,13,17], G. Nicolini[1],
M. Pancrazzi[1], M. Romoli[16,17], C. Sasso[2], A. Slemer[13], M. Stangalini[18], and L. Teriaca[19]

1 INAF – Osservatorio Astrofisico di Torino, Turin, Italy
  e-mail: alessandro.bemporad@inaf.it
2 INAF – Osservatorio Astronomico di Capodimonte, Salita Moiariello 16, 80131 Naples, Italy
3 INAF – Osservatorio Astrofisico di Catania, Catania, Italy
4 Solar-Terrestrial Centre of Excellence – SIDC, Royal Observatory of Belgium, Brussels, Belgium
5 Institute of Geodynamics of the Romanian Academy, Bucharest, Romania
6 Skobeltsyn Institute of Nuclear Physics, Moscow State University, 119992 Moscow, Russia
7 KU Leuven, Leuven, Belgium
8 Naval Research Laboratory, Washington, DC, USA
9 Astronomical Institute, Slovak Academy of Sciences, Tatranská Lomnica, Slovakia
10 Faculty of Education, University of Ljubljana, Ljubljana, Slovenia
11 Faculty of Mathematics and Physics, University of Ljubljana, Ljubljana, Slovenia
12 Astronomical Institute of the Czech Academy of Sciences, Ondřejov, Czech Republic
13 CNR – Istituto di Fotonica e Nanotecnologie, Padua, Italy
14 INAF – Osservatorio Astronomico di Trieste, Trieste, Italy
15 Università di Padova – Dip. Fisica e Astronomia "Galileo Galilei", Padua, Italy
16 Università di Firenze – Dip. Fisica e Astronomia, Florence, Italy
17 INAF – Associate Scientist, Italy
18 Agenzia Spaziale Italiana, Roma, Italy
19 Max-Planck-Institut für Sonnensystemforschung, Göttingen, Germany

ABSTRACT

Context. On 2021 February 12, two subsequent eruptions occurred above the western limb of the Sun, as seen along the Sun-Earth line. The first event was a typical slow coronal mass ejection (CME), followed ~7 h later by a smaller and collimated prominence eruption, originating south of the CME, followed by a plasma blob. These events were observed not only by the SOHO and STEREO-A missions, but also by the suite of remote-sensing instruments on board Solar Orbiter.
Aims. We show how data acquired by the Full Sun Imager (FSI), the Metis coronagraph, and the Heliospheric Imager (HI) from the Solar Orbiter perspective can be combined to study the eruptions and different source regions. Moreover, we show how Metis data can be analyzed to provide new information about solar eruptions.
Methods. Different 3D reconstruction methods were applied to the data acquired by different spacecraft, including remote-sensing instruments on board Solar Orbiter. Images acquired by the two Metis channels in the visible light (VL) and H I Ly-α line (UV) were combined to derive physical information about the expanding plasma. The polarization ratio technique was also applied for the first time to Metis images acquired in the VL channel.
Results. The two eruptions were followed in 3D from their source region to their expansion in the intermediate corona. By combining VL and UV Metis data, the formation of a post-CME current sheet (CS) was followed for the first time in the intermediate corona. The plasma temperature gradient across a post-CME blob propagating along the CS was also measured for the first time. Application of the polarization ratio technique to Metis data shows that by combining four different polarization measurements, the errors are reduced by ~5−7%. This constrains the 3D plasma distribution better.

Key words. Sun: atmosphere – Sun: UV radiation – Sun: corona – Sun: coronal mass ejections (CMEs)

1. Introduction

Space-based coronagraphs are currently the main available tools for continuously monitoring the intermediate solar corona (see, e.g., Hochedez et al. 2005). Images acquired by these instruments provide unique input for the release of the first

alert and forecasting of the occurrence of prominence eruptions and coronal mass ejections (CMEs) and their possible impact on the Earth's magnetosphere (see the review by Webb & Howard 2012). Over the past decades, many space-based coronagraphs allowed us to continuously monitor CMEs and to study their early evolution from ~1.5 to ~30 $R_\odot$ over more than two solar cycles (Yashiro et al. 2004; Gopalswamy et al. 2009), and more than 4×10^4 CMEs have been observed by

---

* Movies associated to Figs. 4–7 are available at
https://www.aanda.org

these instruments (Lamy et al. 2019). The more recent multi-spacecraft coronagraphic observations provided by the STEREO mission also allowed (in combination with data acquired by other instruments) investigating and unveiling the 3D structure of CMEs, which can be now reconstructed with many different forward- and backward-modeling techniques (see the review by Thernisien et al. 2011, and references therein).

With the launch of the Solar Orbiter spacecraft (Müller et al. 2020) in February 2020, a new era of space-based coronagraphy started: the era of multiband coronagraphy. In particular, the Metis coronagraph (Antonucci et al. 2020) on board Solar Orbiter is the first instrument that simultaneously observes in the polarized visible light (VL) broadband in the interval 580–640 nm, and in the UV narrow-band centered around the 121.6 nm Ly-α line emitted by neutral H atoms (the most intense line in the UV solar spectrum). A combined analysis of VL and UV data can provide 2D maps of the electron density and temperature inside CMEs (Bemporad et al. 2018), thus allowing us to study the thermodynamical evolution of CMEs during their early expansion phases for the first time (e.g., Susino & Bemporad 2016). These types of observations might be decisive to finally understand the physical origin of the mysterious additional heating source observed by the UV Coronagraph Spectrometer (UVCS; Kohl et al. 1995) on board SOHO and reported by many previous authors (see Wilson et al. 2022, and references therein). A comprehensive review of CME observations with UVCS can be found in Kohl et al. (2006), while a catalog was compiled by Giordano et al. (2013).

Unlike coronagraphs, space-based extreme-UV (EUV) imagers are the only instruments capable of providing unique information about the pre-CME evolution in their source regions and their early evolution in the inner corona (Georgoulis et al. 2019), as well as the evolution of related phenomena (Hudson & Cliver 2001; Zhukov 2007), such as the so-called EUV waves (see review by Liu & Ofman 2014), EUV dimmings (e.g., Zhukov & Auchère 2004), post-eruption arcades (Tripathi et al. 2004), and CME-driven shocks (see, e.g., Shen & Liu 2012; Mancuso et al. 2019). In this way, EUV images help identify the most probable source of type II radio bursts and acceleration of solar energetic particles (SEPs; e.g., Frassati et al. 2019; Kozarev et al. 2015). These instruments were used for a long time, in combination with photospheric magnetometers, to identify possible precursors or progenitors of CMEs and flares (see the review by Chen 2011). Moreover, since the launch of the STEREO mission, the CME origins in the inner EUV corona can now also be imaged from perspectives different than the Sun-Earth line. The Full Sun Imager (FSI), a telescope of the EUI instrument (Rochus et al. 2020) on board Solar Orbiter, added an additional view with images in its 17.4 nm and 30.4 nm channels. A particularly useful aspect of FSI for CME studies is its large 3.8° field of view (FoV), which provides ample overlap with the Metis FoV (see Auchère et al. 2020).

To track CMEs farther away from the Sun, space-based heliospheric imagers such as SMEI (Jackson et al. 2004) and STEREO/HI (Howard et al. 2008) became a fundamental platform for understanding the Sun-to-Earth propagation of any solar disturbance, such as the interplanetary counterpart of CMEs (ICMEs). These instruments became the baseline for our understanding of the evolution of ICMEs and their associated shocks, as well as for the prediction of their arrival times on Earth and their possible geo-effectiveness (see the recent review by Temmer 2021).

This capability is now being further enhanced by the Solar Orbiter Heliospheric Imager (HI; Howard et al. 2020). HI is comprised of four separate advanced pixel sensor (APS) detectors that are combined to form a single optical system observing the heliosphere in white light. The instrument has a 40° FoV, typically centered near 0° in latitude and 25° elongation from the Sun. HI is on the anti-ram side of the spacecraft, meaning that in a nominal observing configuration for the spacecraft, HI always observes off the east limb of the Sun.

We analyze the observations of three subsequent solar eruptions acquired by the above remote-sensing instruments on board Solar Orbiter. After describing the events as observed by well-established instruments to introduce the main ongoing phenomena (Sect. 2), we describe the images acquired by the EUI (Sect. 3.1), Metis (Sect. 3.2), and HI (Sect. 3.3) instruments in more detail. The combination of these data allowed us to determine the 3D kinematics of the eruptions, as discussed in Sect. 4. Finally (Sect. 5), the Metis polarized images acquired with the VL channel are analyzed and inverted with the so-called polarization ratio technique (Moran & Davila 2004). Results are then summarized in the conclusions (Sect. 6), and we also discuss the advantages of the Metis coronagraph with respect to previous similar instruments.

2. Observations from the Sun-Earth line and STEREO-A

On 2021 February 12, two subsequent eruptions occurred above the west limb as seen along the Sun-Earth line. The complex sequence of events is shown in Fig. 1 with regular (top) and running-difference (bottom) images. The first event appeared in the SOHO/LASCO-C2 images (Brueckner et al. 1995) as a typical CME that started to appear in the instrument FoV around 12:48 UT. The CME propagated in between two pre-existing coronal streamers that were mostly unaffected by the eruption. The subsequent images (see Fig. 1) show the progressive expansion of the CME front, which enclosed a flux-rope-like structure without any clear CME core. The CME had a projected speed of ~110 km s^{-1}, as provided by the CACTUS catalog (Robbrecht & Berghmans 2004). More refined evaluations, based on LASCO running-difference images, give values of ~80–90 km s^{-1} in the LASCO-C2 FoV and ~110 km s^{-1} when the CME front entered the LASCO-C3 FoV, hence this can be classified as a slow and accelerating event, as also reported by the CDAW CME catalog (Gopalswamy et al. 2009), which provides an average acceleration by 5.8 m s^{-2}.

Accordingly, the CME was not associated with any solar flare, filament eruption, or radio burst, but the EUV images acquired by the PROBA2/SWAP instrument (Berghmans et al. 2006; Seaton et al. 2013) show some activity (formation of posteruption arcades) in a region located around 30°–40° west and 30° south (in the Stonyhurst coordinate system) starting from ~10 UT. This is two hours before the appearance of the CME in the LASCO FoV and is outlined in Fig. 2 (third panel). This is the most likely location of the CME source region, as also supported by the EUV full-disk images acquired by the STEREO-A/EUVI instrument (Howard et al. 2008) in the 17.1 nm channel. In particular, on 2021 February 13, at 00:00 UT, the STEREO-A spacecraft was located at a separation angle with the Earth of 55.86° east (see Fig. 3), and from this vantage point, the spacecraft observed the off-limb early propagation phase of the CME, appearing at 10:09 UT as a loop arcade expanding from the west limb close to the instrument plane-of-sky. The footpoints of the expanding arcade were located around ~20° south and ~40° south (see Fig. 2, right panel) in the Stonyhurst coordinates.
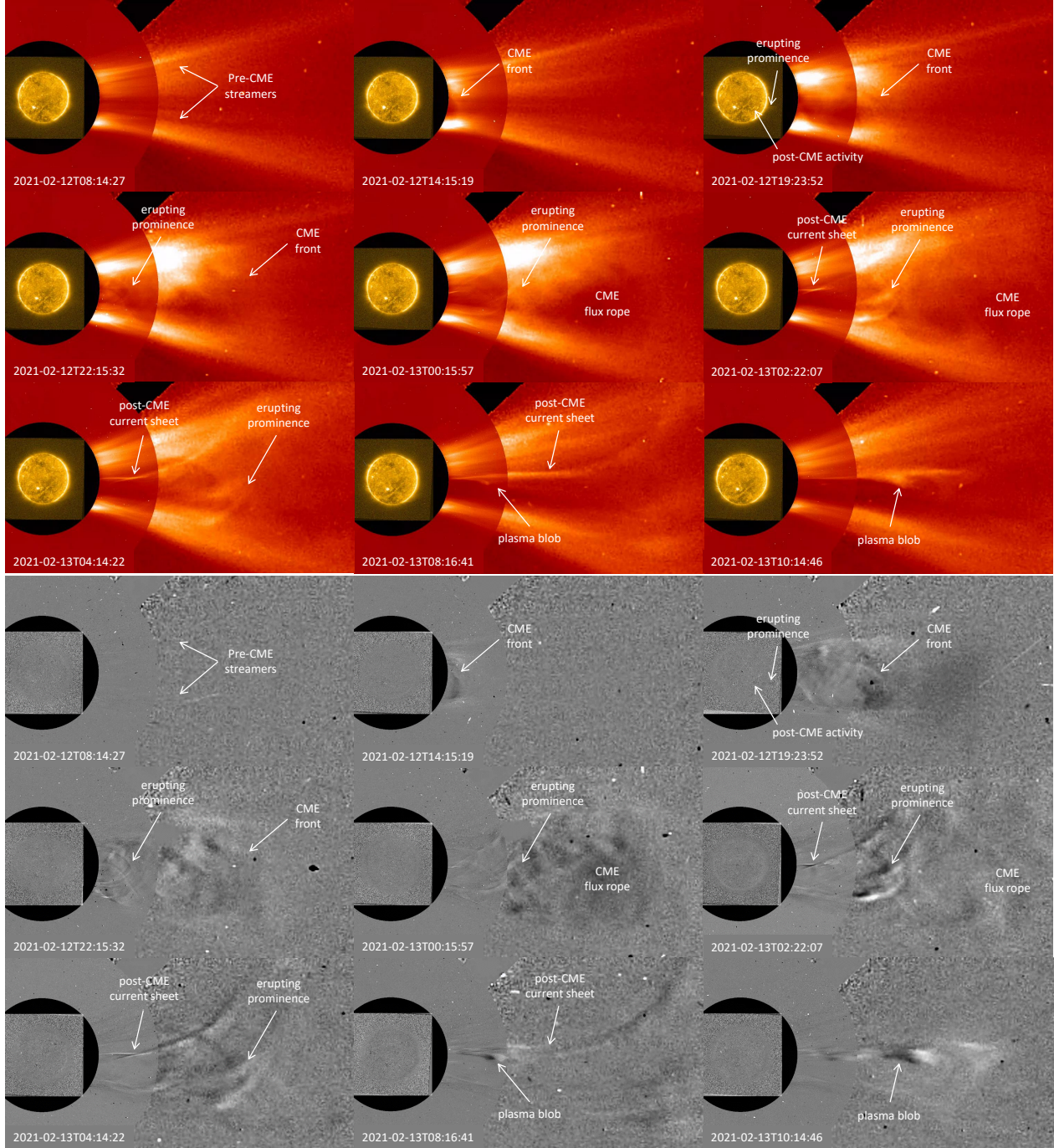
Fig. 1. Complex sequence of events between 2021 February 12 and 13 as shown by the PROBA2/SWAP imager and SOHO/LASCO-C2 and C3 coronagraphs (see text). The *top panel* shows intensity images, and the *bottom panel* shows the corresponding running difference images. All these combined images have been created with JHelioviewer (Müller et al. 2017).

This slow CME was followed by a complex sequence of two small-scale events. First, as observed from the ground by the K-Cor coronagraph at the Maunaloa Solar Observatory (ML) and the Global Oscillation Network Group Hα network monitor operated by the National Solar Observatory, (NSO-GONG, Harvey et al. 2011), a prominence following the CME started to erupt on February 12 around 18:00 UT, leaving the instrument FoV around 21:00 UT (see Fig. 4 and relevant data[1]). The prominence appeared to leave the solar limb as seen from the Earth

from a projected latitude of about 25° S, propagating mostly toward the equatorial plane. The initial projected propagation speed of the prominence is low, about $22\,\mathrm{km\,s^{-1}}$ as measured with K-Cor images, but the prominence slowly accelerated up to a speed of about $51\,\mathrm{km\,s^{-1}}$ when it left the instrument FoV. During its early expansion phase, the prominence clearly assumed a hook-like shape, as shown in detail in the third bottom panel in Fig. 4 acquired at 20:01 UT. This apparent shape is likely related to twisting motions that occur in the early expansion phases: the Hα images, acquired at earlier times at the Kanzelhöhe Observatory (KO; Pötzi et al. 2015) and by the NSO-GONG network

---

[1] https://search.datacite.org/works/10.5065/d69g5jv8
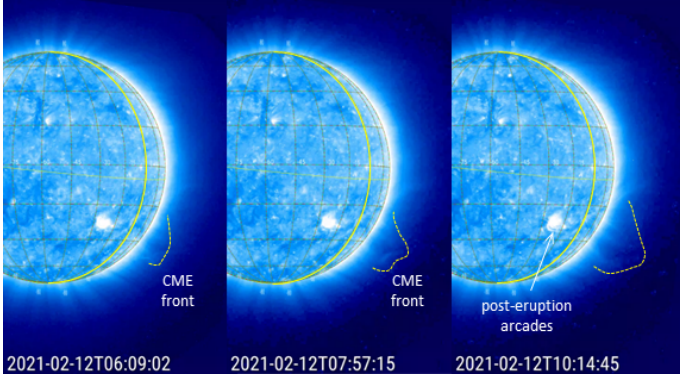
Fig. 2. Early expansion of the CME front as observed at the beginning of February 12 in the STEREO-A/EUVI 17.1 nm channel (see text). The solid yellow line shows the location of the central meridian as seen from Earth, and the latitude and longitude grid coordinates are given in the Stonyhurst reference frame.
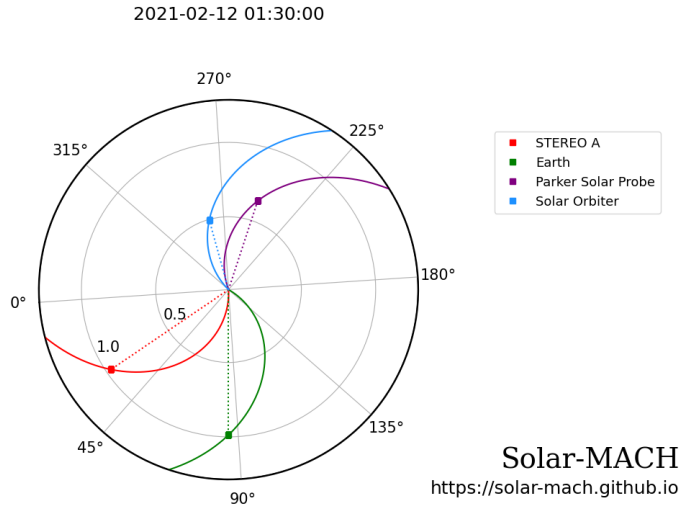
Fig. 3. Locations of the different spacecraft and Earth between 2021 February 12–13, as seen projected onto the ecliptic plane.

monitors (Fig. 5), show that the prominence rotated around a vertical axis during the outward propagation, and changed its orientation from mostly east-west to mostly north-south. Interestingly, the K-Cor images also show that starting from ∼21 UT, the northern leg of the prominence leaves the Sun. This resulted in an almost radial intensity enhancement, while its southern leg material was apparently deposited in the surrounding corona.

Associated with the prominence, the PROBA2/SWAP instrument also simultaneously detected an expanding tongue of plasma, outlined in Fig. 1 (top right panel), that was also observed by the SDO/AIA telescopes. Hence, higher up in the LASCO-C2 FoV, this eruption resulted in more filamentary plasma features following the CME (Fig. 1, middle row panels). The clear identification of features observed in the coronagraphs with the prominence is complicated by the occurrence of the nearby CME, which was partially aligned along the line of sight (LoS), and also because by the described prominence twisting motions observed in the low corona which probably proceed higher during the expansion. The prominence, propagating at about 80 km s^{-1} in the LASCO FoV, finally merged with the post-CME plasma, becoming nearly indistinguishable from

the CME in the LASCO-C3 FoV. The observations of the same prominence by Solar Orbiter/FSI is discussed below.

After the CME and the prominence, the LASCO images show the propagation of an inverted V-shape smaller-scale intensity enhancement (Fig. 1, middle row panels), resulting in a radial coronal feature (aligned with the CME propagation latitude) that we identify here as the post-CME current sheet (CS). This identification is supported by and discussed below based on Metis observations. Moreover, after the CME and the prominence, the LASCO images also show the expansion of a collimated plasma blob that is almost coaligned with the post-CME CS, and propagates much faster at a projected speed of ∼380 km s^{-1} (see Fig. 1, middle and right bottom panels) in the LASCO/C2 FoV. It therefore rapidly merges later on with the slow CME and with the prominence that propagated ahead. The origin of this post-CME blob is more uncertain because no clear activity was observed by the SDO/AIA and PROBA2/SWAP full-disk imagers. The study of this blob with Solar Orbiter/Metis data is also discussed below.

When we consider the small separation angle between the apparent source regions of the CME (Fig. 1, top panels) and the prominence eruption (Fig. 4) and their time sequence, these two events might be candidates for sympathetic eruptions (see the review by Lugaz et al. 2017). The first event (a typical slow CME with a front and a cavity, but no clear core) possibly destabilizes a nearby prominence and opens (by some kind of interchange reconnection) the route for its propagation, which finally leads to the prominence eruption that expands near the CME flanks. A similar sequence of events was described, for instance, by Bemporad et al. (2008). The subsequent formation of a post-CME CS (Fig. 1, middle panels) is typical for solar eruptions because these features are thought to form as a consequence of post-CME magnetic reconnection (e.g., Lin & Forbes 2000). This also suggests a possible physical explanation for the subsequent more compact and faster plasma blob (Fig. 1, bottom panels). Because this feature was also apparently aligned with the prominence, it is possible that the blob was accelerated by magnetic reconnection in the reconfiguration phases of the solar corona in the post-CME CS. The formation of similar plasma blobs is typical for the evolution of post-CME CS (e.g., Ko et al. 2003; Vršnak et al. 2009), and is thought to be driven by a tearing instability that is related to the CME expansion (e.g., Shibata & Tanuma 2001; Bárta et al. 2008).

3. Events as observed from Solar Orbiter

In order to understand the different appearance of the events described above as seen from Solar Orbiter, it is important to consider that between 2021 February 12–13, the spacecraft was separated by 161.6° east from the Earth in heliographic longitude (see Fig. 3), hence was mostly observing the opposite solar hemisphere with respect to the Earth. This means that all the events that were observed above the west (east) limb from the Sun-Earth line view are expected to propagate above the east (west) limb as seen from Solar Orbiter.

3.1. EUI observations

We used Release 2 of the calibrated EUI/FSI data[2]. The cadence of the FSI 17.4 nm images was about 30 min (see Fig. 6), and no 30.4 nm images were taken. There is no counterpart of the main slow CME observed in the Metis data, probably because

---

[2] https://doi.org/10.24414/z2hf-b008
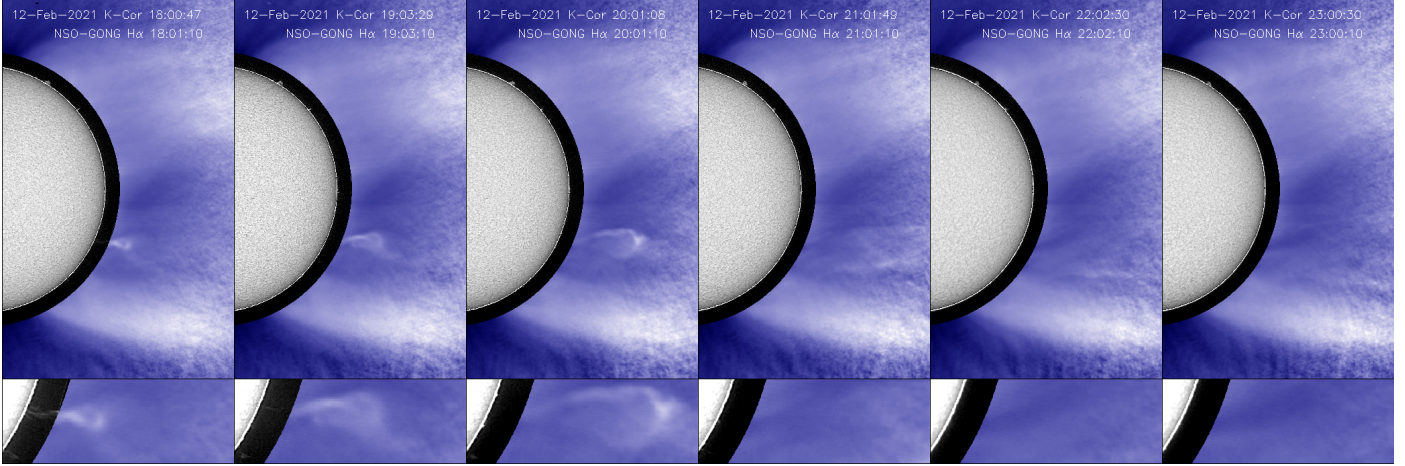
Fig. 4. Prominence eruption as observed in the late hours of February 12 by the K-Cor coronagraph and the NSO-GONG network Hα monitor at the ML (see also Fig. 6). The size of the FoV in the *top and bottom panels* is 1840″ × 3000″ and 850″ × 310″, respectively. The outer radius of the off-limb annulus is about 115″ larger than the solar radius. A movie is available online.

its source region was located on the opposite side of the Sun (see Sect. 2) and because of the low speed of the CME, which does not allow observing the development of coronal dimmings above the limb (Kilpua et al. 2014; Palmerio et al. 2021). The eruption of the prominence, in contrast, was well observed by FSI (Fig. 6). The corresponding structure (bright in the 17.4 nm passband) above the east limb slowly rose, starting from about 16:15 UT on February 12. By 18:15 UT, a concave-out structure is formed, which evolves to the hook-like morphology seen at 19:45 UT. The hook-like structure rises with an average speed of ~40 km s^{-1}, becoming at 22:15 UT difficult to distinguish from compression artifacts in the outer FoV of FSI. The southern leg of the structure can still be seen to rise slowly even early on February 13, while the northern leg has already erupted. No clear coronal dimming was observed.

The origin of the propagating plasma blob observed by LASCO at 08:16 UT (Fig. 1, bottom middle panel) is not seen in the low corona by FSI. As anticipated, this structure was probably formed higher up in the corona in the post-CME CS.

3.2. Metis observations

Between 2021 February 12–13, the Metis coronagraph acquired low-cadence sequences of VL and UV synoptic images. Both instrument detectors were binned with a 2 × 2 binning, resulting in 1024 × 1024 pix^2 VL images and 512 × 512 pix^2 UV images, with spatial scales of 20.3″ pix^{-1} and 40.8″ pix^{-1}, respectively. The Solar Orbiter spacecraft was located at a heliocentric distance of ~0.5 AU, therefore the Sun was observed with an apparent photospheric radius of 1934.52″, and the above projected plate scales correspond on the instrument plane of the sky to about 7300 km pix^{-1} in the VL and 15 000 km pix^{-1} in the UV.

The instrument acquired one full VL polarimetric sequence every hour, consisting of four images at different orientations of the linear polarizer, in parallel with two UV images. Each VL image was obtained by averaging on board 15 frames acquired at the same polarizer orientation with an integration time of 30 s, corresponding to a total effective exposure time of 450 s. However, because Metis polarimetric observations are carried out by cycling over the four specified polarizer orientations for each acquired frame, which results in an interleaved stream of polarimetric frames (see Sect. 9.1 in Antonucci et al. 2020), the
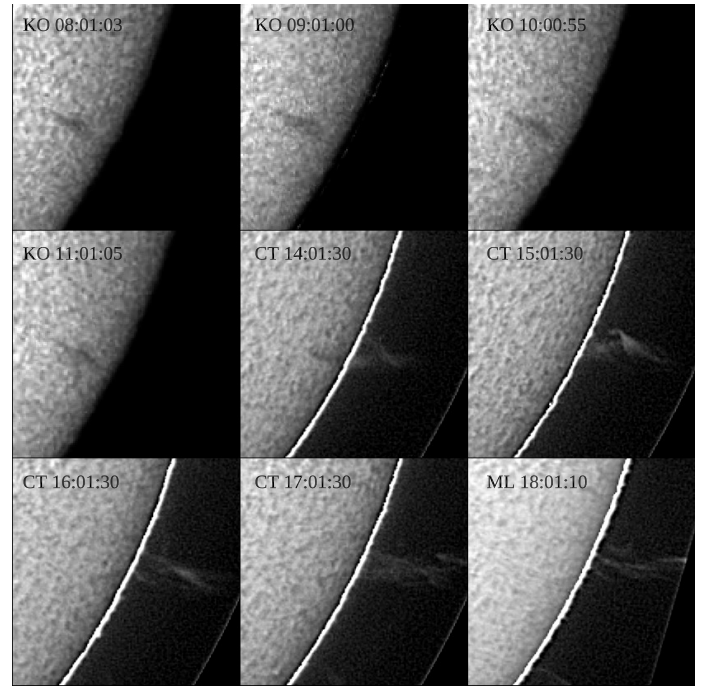
Fig. 5. Prominence eruption as observed from the beginning by the KO and the NSO-GONG network Hα monitors at the CT and the ML. The size of the FoV is 300″ × 300″. A movie is available online

elapsed time between the acquisition of the first and the last frames, corresponding to the same polarizer orientation, is about 30 min, which is nearly equal to the time taken by the acquisition of the full sequence. The UV images were obtained by averaging 15 frames acquired with an integration time of 59.967 s, corresponding to a total effective exposure time of 899.5 s, so that the acquisition of both images required about 30 min.

The data were calibrated by performing standard operations such as bias and dark subtraction, flat-field and vignetting corrections, and exposure-time normalization (see Romoli et al. 2021). The improvements in the UV vignetting function described in Appendix A of Andretta et al. (2021) were also included. Each set of polarimetric VL images was combined using the Müller matrix obtained from laboratory calibrations
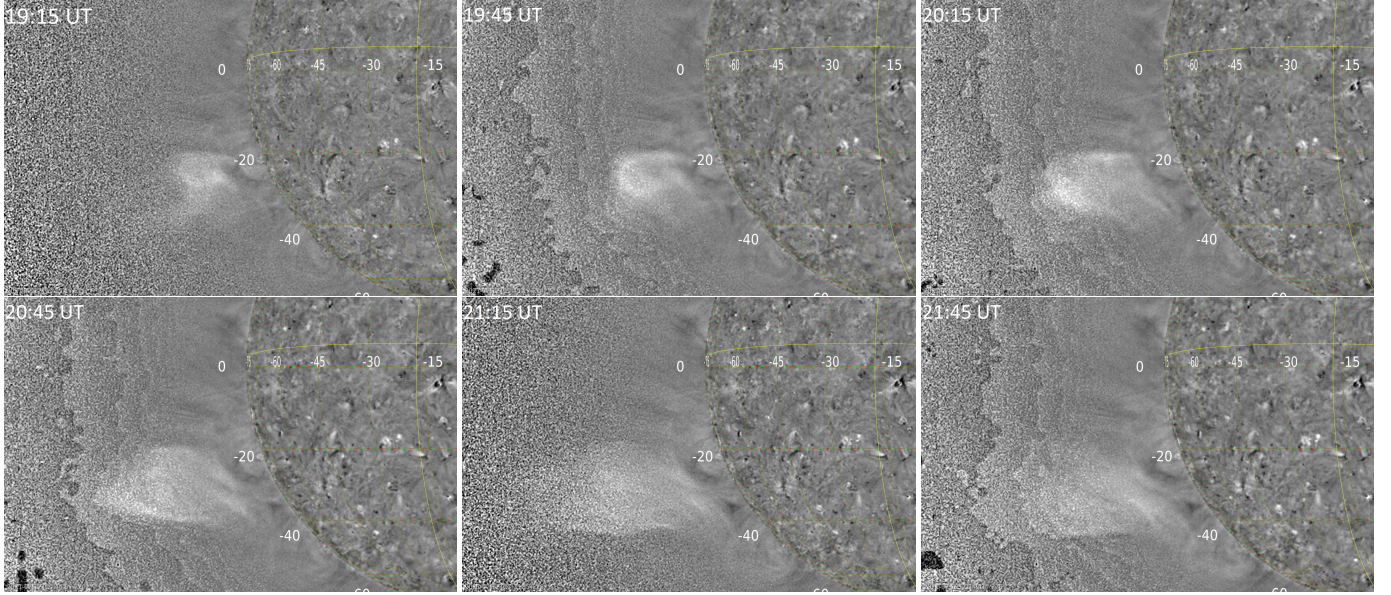
Fig. 6. Eruption of a bright structure (corresponding to the prominence shown in Fig. 4) observed in FSI 17.4 nm base-difference images taken on 2021 February 12 at the different times given in each panel. The image taken at 15:15 UT was subtracted from each of the original images to reveal the evolution of the coronal structure during the eruption. An online movie showing the event is also available. The images and the movie were created with the JHelioviewer software (Müller et al. 2017).

to derive the corresponding total- (tB) and polarized-brightness (pB) images.

It is worth noting that the synoptic program to which the observations presented here belong was primarily designed to monitor the status of the solar corona in a long time interval and to provide additional context data for the joint science with the other Solar Orbiter instrumentation. Acquisitions were therefore not optimized for the study of solar transients and CMEs. For this reason, considering that the acquisition of each VL sequence was approximately twice as long as that of any single UV image, some differences are expected in the appearance of moving features. In particular, given the above pixel scales and acquisition times, a partial blurring in the images is expected for every feature moving faster than $\sim 4 \, \text{km s}^{-1}$ and $\sim 16 \, \text{km s}^{-1}$ in the VL and UV channels, respectively. In order to take the different duration of the UV and VL acquisitions into account, it is possible to average the two subsequent UV images.

Selected VL pB and UV images are shown in the different panels of Fig. 7 (top), in red and cyan, respectively; for each image, the starting acquisition time is given at the top. Similar to Fig. 1, this figure also provides the identification of different features in the regular (top) and running-difference (bottom) images. This figure shows that Metis observed the first CME as a very faint front enclosing a darker cavity, followed by multiple filamentary features without any evident core. The CME appeared to propagate in the Metis FoV above the east solar limb as seen from Solar Orbiter, moving at an apparent projected speed of $\sim 80-100 \, \text{km s}^{-1}$ (a more precise value of this speed is provided below based on 3D reconstructions). After the transit of the CME, the Metis images also show faint filamentary expanding features that resemble those that were observed by LASCO and are likely related with the expansion of the prominence. They are too diluted at these altitudes to produce significant Ly-α emission. The subsequent images also show a radial intensity enhancement associated with the formation of the post-CME CS, and the subsequent trailing plasma blob moving at a projected speed of $\sim 210 \, \text{km s}^{-1}$ (as measured with the two UV

frames acquired at 08:15 and 08:30 UT). All these features (indicated with white arrows in Fig. 1) are also marked in different panels of Fig. 7.

The presence of spatial gradients in the plane-of-sky (PoS) distribution of plasma velocities or temperatures should result in variations in UV intensity distribution with respect to VL, related with the Doppler dimming of UV Ly-α emission or the abundance of neutral H atoms. A comparison between pB and UV images shows no evident differences between the appearance of CME features in the two channels, however, that could suggest such gradients. On the other hand, the bottom left panels of Fig. 7 show very interestingly that the post-CME radial feature that we identified as the CS appears as an intensity enhancement in the VL and an intensity depletion in the UV Ly-α. This difference is better shown in Fig 8, showing a zoom of the coronal regions involved in the formation of this radial feature (left panels), and a vertical (north-south) cut proving the normalized intensity distributions across this feature in the VL (red lines) and in the UV Ly-α (blue lines) before (top right) and after (bottom right) its formation. These observations agree very nicely with what was previously observed with the UVCS instrument (see, e.g., Lin et al. 2005). In particular, the depletion in the Ly-α emission is a signature of higher radial velocities along the CS and higher plasma temperatures, both related to ongoing magnetic reconnection processes, and both resulting in a reduction of the observed Ly-α emission.

In order to compare VL and UV observations of moving features, it is important to take into account that considering the above CME and blob propagation speeds in the Metis FoV during the acquisition times, the observations are expected to be blurred by approximately 24–69 and 6–17 pixels in the VL and UV channels, respectively. These expected blurrings in the VL channel are four times stronger than those in the UV because the VL pixel resolution is twice better than in the UV, and the VL acquisition time is twice as long as the UV. Because the VL acquisition lasted ~ 15 min longer than the UV acquisition, we expect displacements between the VL and UV images by
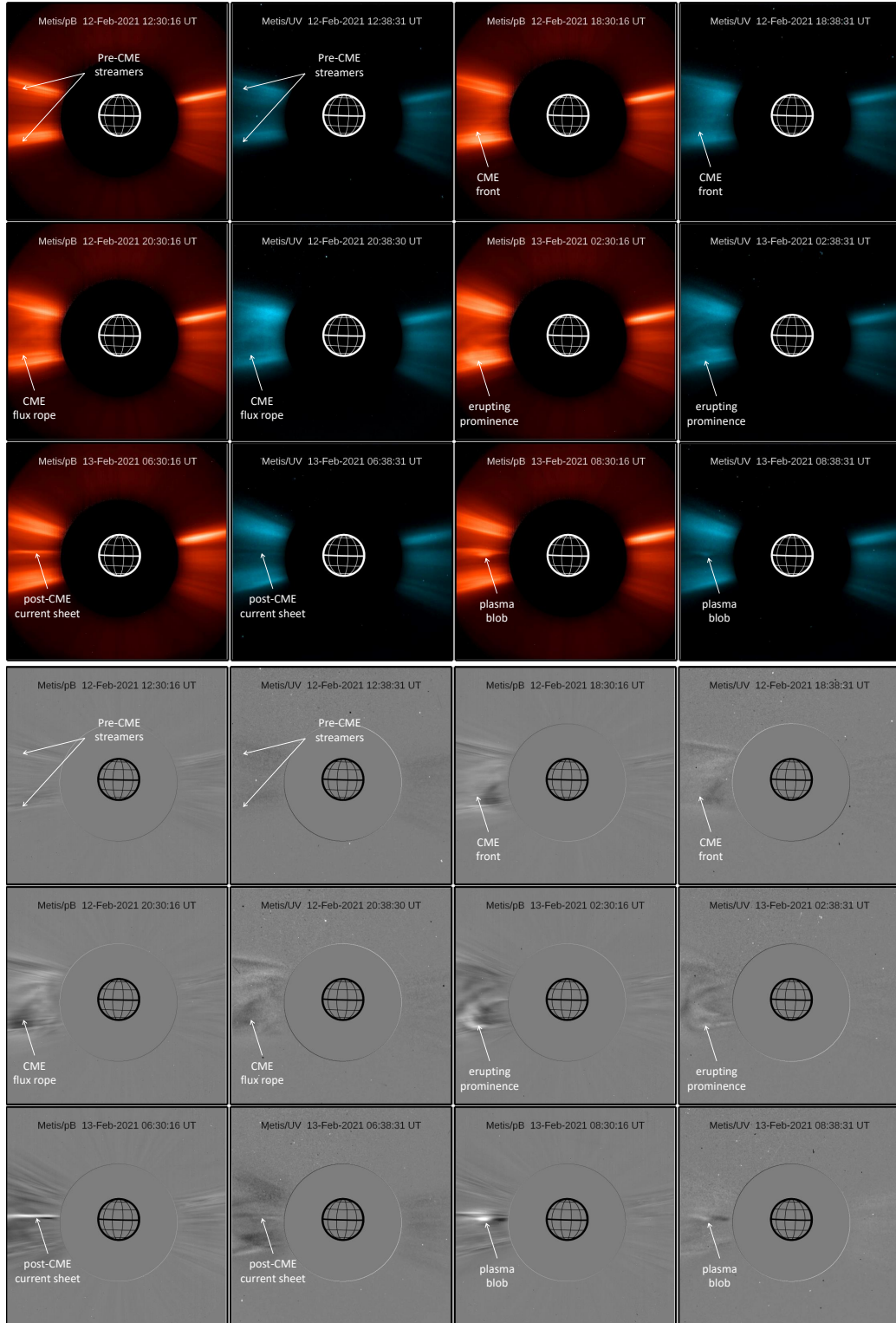
Fig. 7. Sequence of events between 2021 February 12–13, as observed by the Metis coronagraph in the VL (red) and UV (cyan) channels (see text). The *top panel* shows regular intensity images, and the *bottom panel* shows the corresponding running-difference images. A movie is available online

$\sim 0.13\,R_\odot$ and $\sim 0.30\,R_\odot$ for the CME and the blob, respectively. We also recall that the effective Metis spatial resolution of the UV channel is degraded to 80″ pix^{-1} (Antonucci et al. 2020).

To reduce differences related to the different acquisition time intervals, it is sufficient for this sequence to average the two successive UV frames to cover the same acquisition time in the UV that is covered by one full VL polarized observation, and avoid possible differences related with plasma motions. As an example, by averaging the two UV images acquired between 08:15–08:30 UT and 08:31–08:46 UT, it is possible to perform a comparison between the VL and UV normalized light distributions across the post-CME plasma blob, as is shown in Fig. 9,
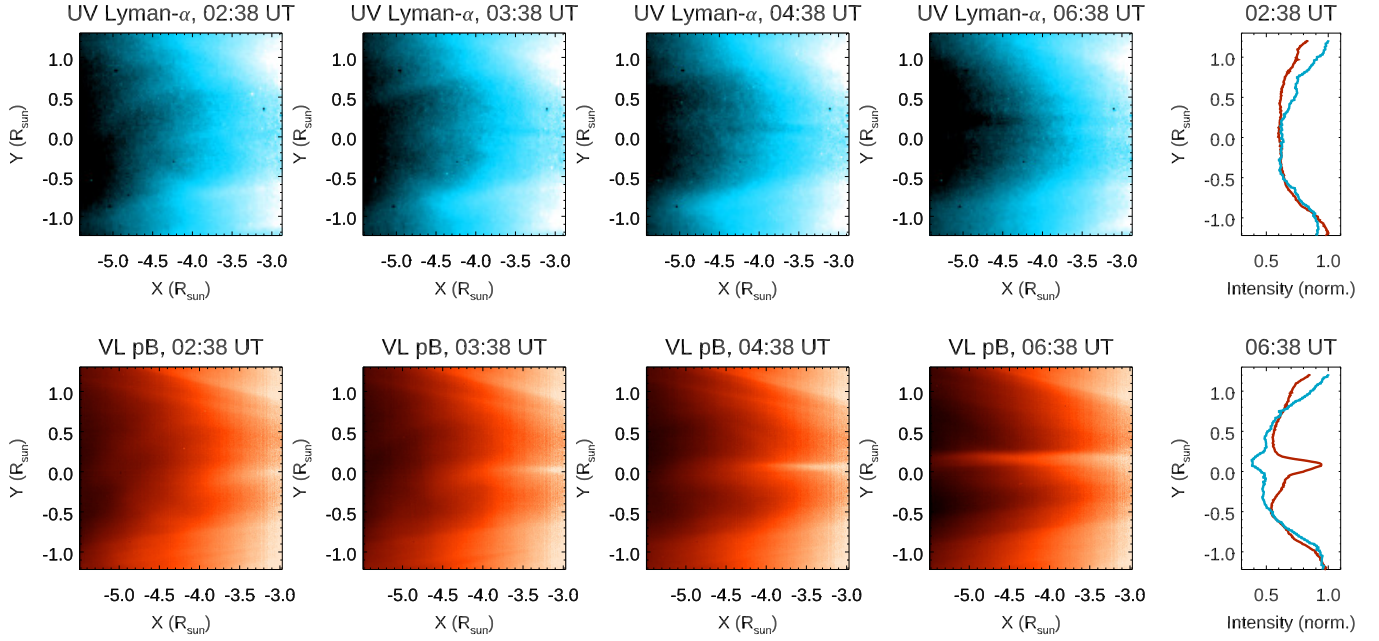
Fig. 8. The formation of the post-CME CS as observed by the two Metis channels. *Left:* zoom over the post-CME CS as observed by Metis on February 13 between 02:38 and 06:38 UT in the UV (*top*) and the VL (pB, *bottom*) channels (see also the bottom right panel of Fig. 7). *Right:* normalized UV (blue) and VL (red) north-south intensity profiles as obtained at 02:38 UT (*top*) and 06:38 UT (*bottom*) by averaging east-west between $-5.4\,R_\odot$ and $-4.4\,R_\odot$ (see text for explanations).
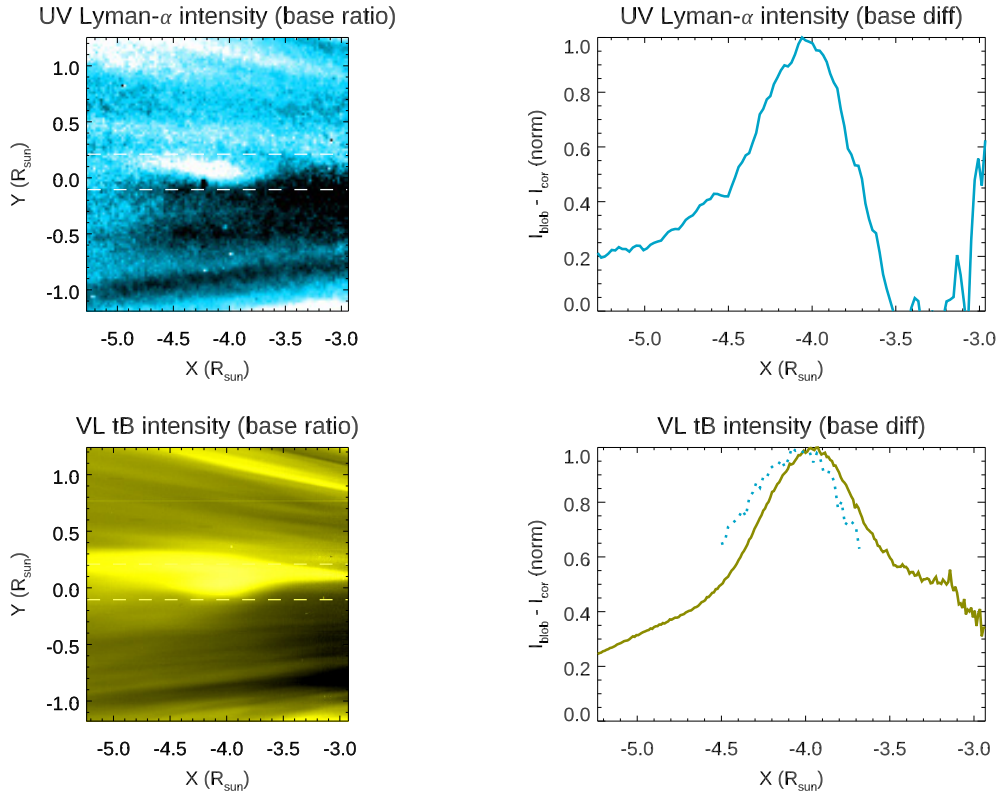
Fig. 9. Propagation of the post-CME plasma blob as observed by the two Metis channels. *Left:* zoom of the expanding small-scale post-CME plasma blob observed by Metis on February 13 between 08:15 and 08:46 UT in the UV (*top*) and the VL (tB, *bottom*) channels (see also the bottom right panel of Fig. 7). These images are obtained from the ratio of the actual frames and those acquired between 12:15 and 12:46 UT on February 12; the horizontal dashed lines mark the area in which the VL and UV intensities have been averaged to create the east-west profiles shown in the right panels. *Right:* normalized UV (*top*) and VL (tB, *bottom*) east-west intensity profiles as obtained by averaging north-south over the areas shown with horizontal dashed lines in the left panels. These profiles are obtained after a subtraction of the actual frames and those acquired between 12:15 and 12:46 UT on February 12. The dotted line in the bottom right panel shows a comparison to the square root of the UV profile shown in the top right panel (see text for explanations).

which is also to be compared with the bottom right panel of Fig. 7. The resulting radial distribution of the plasma blob emission appears to be broader in VL than in the UV image, where the blob extension is instead more limited (Fig. 9, right panels). In particular, the blob in the radial direction has an extension of $0.60\,R_\odot$ in VL and $0.48\,R_\odot$ in UV (by measuring the extension within 75% of the intensity peak). Moreover, the blob in the UV appears to be radially shifted with respect to the VL by about $0.15\,R_\odot$. These interesting differences between the VL and UV light distributions can be explained as discussed below.

A comparison between different VL and UV frames acquired during the blob propagation shows that its radial extension did not increase significantly with time. In particular, from the analysis of the LASCO/C2 frames acquired on February 13 at 08:12 UT and 08:48 UT, it turns out that in this time interval the blob expanded radially by no more than $\sim 0.09\,R_\odot$ (corresponding to a projected expansion speed by $\sim 29\,\mathrm{km\,s^{-1}}$), propagating radially by $0.42\,R_\odot$ (corresponding to a projected propagation speed of $135\,\mathrm{km\,s^{-1}}$). Hence, the blob appeared to propagate with a very limited radial expansion rate ($\sim 20\%$), which means that the radial speed distribution across the blob can be considered constant. As a consequence, no significant radial variations of the Ly-α emission across the blob are expected because of the Doppler dimming effect. Moreover, when we consider that the unprojected propagation speed of $\sim 210\,\mathrm{km\,s^{-1}}$ corresponds to a normalized Ly-α Doppler dimming factor ~ 0.3 (see, e.g., Capuano et al. 2021, Fig. 3), and when we consider that the blob is brighter in the VL hence has also a higher plasma density, the observed Ly-α intensity increase associated with the blob is expected to be mainly due to collisional rather than radiative excitation of H atoms, similarly to what has previously been discussed by Bemporad et al. (2018) for the Ly-α observations of CME cores. Because the collisional component of the EUV-UV emission lines is roughly proportional to the square of the plasma density while the VL emission is roughly proportional to the density, this could also explain why the radial extension of the UV blob appears much more limited than what is observed in VL.

To support this interpretation, the right panels of Fig. 9 show the normalized radial intensity distributions across the blob as obtained after subtraction of the pre-CME images for the UV (top) and VL (bottom, solid line) acquired between 12:15 and 12:46 UT on February 12, as well as the square root of the UV distribution (bottom, dotted line). The square root of the normalized UV intensity profile appears much more similar to the VL intensity profile, supporting the interpretation that the UV emission is mostly collisional, but the evident shift by $\sim 0.15\,R_\odot$ between the two profiles requires a different explanation. This effect can be interpreted instead as an interesting signature of a temperature gradient across the blob. In particular, when we assume that the ascending top fraction of the plasma blob at $4.5\,R_\odot$ has a typical coronal streamer temperature at this altitude by 1.0×10^6 K (see e.g., Vásquez et al. 2003), a gradual temperature increase across the blob up to $\sim 1.55 \times 10^6$ K at $3.9\,R_\odot$ could explain the observed apparent shift between the UV and VL profiles, as determined with the H ionization equilibrium curve provided by the CHIANTI spectral code (Dere et al. 2019). This temperature increase corresponds to a decrease in the density of neutral H atoms by about a factor 1.6: once the normalized VL and UV profiles in the bottom right panel of Fig. 9 are equalized at $4.5\,R_\odot$, this factor allows us to reproduce the UV to VL intensity jump at $3.9\,R_\odot$. We also note that any possible radial variation of the Ly-α Doppler dimming coefficient across the blob due to its radial expansion (neglected in the temperature estimate)

would lead to a shift between the VL and UV emissions opposite to what is observed (bottom right panel of Fig. 9), by more significantly reducing the Ly-α intensity in the blob regions located at higher altitudes and moving faster, and vice versa. The possible physical explanation for this temperature gradient across the blob is discussed in the last paragraph.

3.3. HI observations

During the period of February 12–14, HI was performing a test observing program with a 2-h cadence on a single tile (Tile 1) of the detector. This is the bottom right tile in the overall mosaic, providing coverage of roughly 5°–25° in elongation and −20°–0° in latitude. This coverage was sufficient to observe much but not all of the CME front and associated material observed in Metis. In particular, Fig. 10 shows a series of snapshots of the HI observations between February 12 and 14. The images were processed to minimize the F-corona and highlight the small solar outflows visible in HI before the CME appears. The front of the CME enters the instrument FoV just after 00:00 UT on February 13. Complex structures are visible behind the leading edge, likely corresponding to the CME flux rope and outflows associated with the restructuring behind the CME. This is shown in Fig. 7.

A distinct structure is visible around 10:00 UT on February 13, although it does not become easily isolated until 18:24 UT. This is thought to be related to the eruptive prominence seen in Metis at 06:30 UT. Behind it, a small blob is also observed, which likely is the HI counterpart of the plasma blob highlighted in Fig. 7 at 08:30 UT in Metis.

To better illustrate the connection between structures seen in Metis and those observed in HI, a J-map or height time plot featuring data from both instruments is shown in Fig. 11, built by extracting intensity slices at position angle of 94° or 4° below the equatorial plane. The map has a gap of approximately 2° in elongation between Metis and HI, but even without direct overlap of each FoV, it is possible to relate the features seen in each instrument in a manner consistent with a streamer blowout CME that has a gradual rise phase in the Metis FoV before it is accelerated to a more constant speed in HI. The CME front in Fig. 11 is denoted with a red line and corresponds to a profile with an average speed of $\sim 250\,\mathrm{km\,s^{-1}}$ throughout the combined FoV. Everything between the red and green lines is considered to be either part of the CME flux rope or an associated outflow. The eruptive prominence is marked with the blue line and corresponds to a slower speed of $\sim 170\,\mathrm{km\,s^{-1}}$.

4. Reconstructions with multiple observations

In order to identify the source regions of the events described above and their subsequent evolution, we applied different reconstruction techniques to derive their 3D positions, namely, the graduated cylindrical shell (GCS) model (see e.g., Thernisien et al. 2009; Thernisien 2011) for the main CME, and triangulation (Inhester 2006) for the erupting prominence.
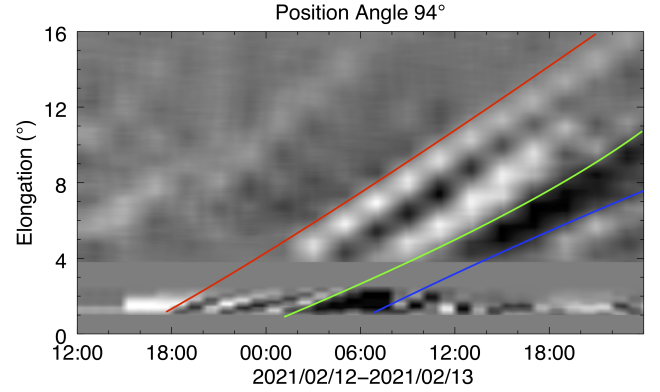
The GCS model is meant to reproduce the large-scale structure of flux-rope-like CMEs. It consists of a tubular section forming the main body of the structure that is attached to two cones that correspond to the legs of the CME. Only the surface of the CME is modeled, and its internal structure is not rendered. This gives us information mostly about the propagation of the leading edge of the CME. The model fits the geometrical structure of CMEs as observed by different white-light coronagraphs. The output of the model is the propagation longitude and latitude, the
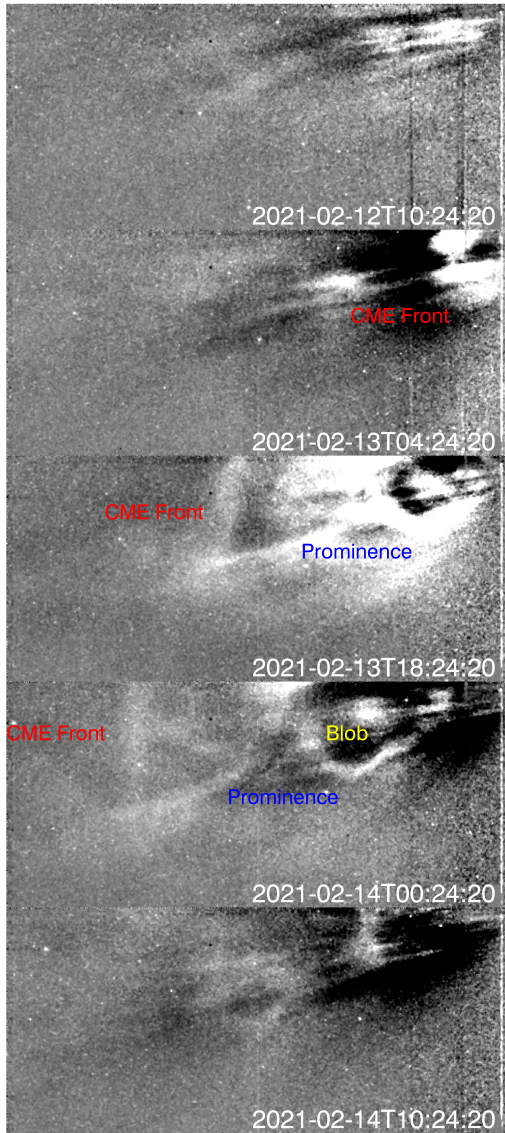
Fig. 10. Series of HI still frames showing the passing of the CME through Tile 1. Each frame is a cropped area of the full detector and corresponds to all 2048 pixels in the *x*-direction and the top 920 detector pixels in the *y*-direction. The CME front is labeled in red in the three frames where it is visible. The eruptive prominence (blue) and the following plasma blob (yellow), corresponding to structures in Metis (Fig. 7), are also shown.

Fig. 11. Combined Metis and HI J-map at position angle 94°. The CME front (red), trailing edge (green), and the later eruptive prominence (blue) are all denoted with lines on the plot. The HI FoV was cropped to 16° in elongation to allow the Metis FoV from ~1.25° to 3° to be seen better.

half-angular width, the aspect ratio, the tilt angle with respect to the solar equator, and the leading-edge height of the CME. The fitting can be made for multiple consecutive time steps in the corona giving the height and time profiles and the evolution of the CME geometrical and kinematic parameters in the corona.

We performed the GCS fitting for the CME observed by Metis at 15:15, 16:15, and 17:17 UT (see Fig. 12, right panels). The corresponding LASCO-C2 and COR2-A images were taken at 15:22, 16:22, and 17:22 UT (Fig. 12, left panels) and at 15:24, 16:24, and 17:24 UT (Fig. 12, middle panels), respectively. As the light travels in about four minutes from Solar Orbiter to Earth and STEREO-A, these images were taken 3 min (LASCO-C2) and 5 min (COR2-A) later than the corresponding Metis images. The results of the GCS reconstruction are provided in Table 1 in the Stonyhurst coordinate system.

The CME propagates in a radial direction along a longitude by 60° west and a latitude by 6° south. These coordinates agree well with the location of the possible source region as observed by the PROBA2/SWAP and STEREO/EUVI instruments at approximately ~20°–30° eastward and ~24° southward (see Sect. 2), indicating that in the early propagation phases, the CME expanded more westward and northward. This nonradial expansion is also clearly suggested by the different locations of the EUV front as outlined in the sequence of STEREO/EUVI images (yellow lines in Fig. 2). Moreover, the height values provided in Table 1 correspond to an average radial speed of approximately 60 km s^{-1}, which is even lower than previous estimates based on single images acquired by the LASCO and the Metis coronagraphs. These differences are likely related to the weakness of the CME front emission, which leads to uncertainties in the position tracking that can be mitigated only by using multiple view-point observations. It is important to note as well that with such a low speed, no significant Doppler dimming effect is expected in the Ly-α emission observed by Metis. This explains the similarity between CME coronagraphic images acquired in the VL and UV channels (Fig. 7).

We also performed triangulation on the leading edge of the erupting prominence observed by FSI 17.4 nm at 19:15 UT and by SWAP at 19:18 UT. The triangulation method requires identification of the same point in the two images (a process called tie-pointing; see, e.g., Inhester 2006). Moreover, the method can only be applied to relatively smaller-scale and compact features (e.g., prominences or blobs) because a point-like geometry needs to be assumed as well (Liewer et al. 2011). This assumption is valid in this case, also because the separation angle between the SWAP and FSI LoS was small (18°), and by tracking the outermost bright region of the prominence, the errors are minimized. The 3D positions of the LoS passing through the point that is visible in the two images were calculated, and the position of the intersection point in 3D space was determined. We performed the triangulation on the outermost bright point of the leading edge of the prominence observed by FSI and SWAP using the *scc_measure.pro* program of SolarSoft (Thompson & Reginald 2008; Thompson 2009), which outputs the position of the feature in Stonyhurst coordinates (longitude, latitude, and height from the center of the Sun; see Thompson 2006).

The images recorded at the time mentioned above showed the erupting prominence in the FSI and SWAP FoV best. Later
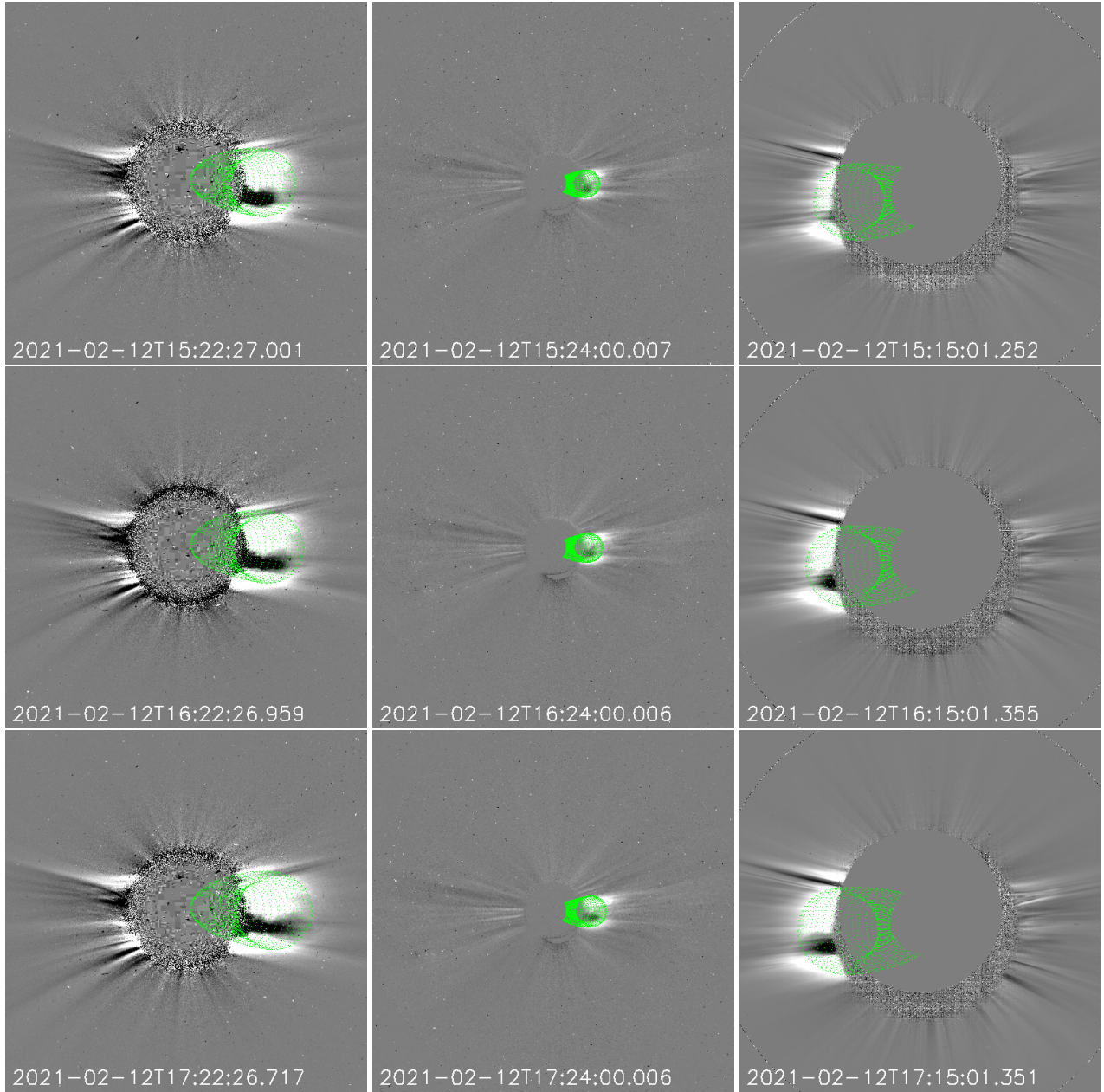
Fig. 12. The February 12 CME as observed by coronagraphs on board different spacecraft at different times. *Upper row*: GCS reconstruction of the CME on February 12 observed by LASCO-C2 at 15:22–07:58 UT (*left panel*), by COR2-A at 15:24–08:24 UT (*middle panel*), and by Metis at 15:15–12:15 UT (*right panel*). *Middle row*: GCS reconstruction of the CME on February 12 observed by LASCO-C2 at 16:22–07:58 UT (*left panel*), by COR2-A at 16:24–08:24 UT (*middle panel*), and by Metis at 16:15–12:15 UT (*right panel*). *Lower row*: GCS reconstruction of the CME on February 12 observed by LASCO-C2 at 17:22–07:58 UT (*left panel*), by COR2-A at 17:24–08:24 UT (*middle panel*), and by Metis at 17:15–12:15 UT (*right panel*).

Table 1. 3D CME parameters as derived from the GCS fitting.

CME Date and time (yyyy-mm-dd hh:mm)	Longitude (°)	Latitude (°)	Tilt angle (°)	Height ($R_\odot$)	Ratio	Half angle (°)
2021-02-12 15:15	W 60	S 06	0	4.042	0.4	30
2021-02-12 16:15	W 60	S 06	0	4.328	0.4	30
2021-02-12 17:15	W 60	S 06	0	4.642	0.4	30

Notes. Column (1): date and time of the reconstruction in Metis. Columns (2) and (3): longitude and latitude of the CME as observed from the Earth. Column (4): tilt angle with respect with the solar equator. Column (5): height of the CME measured from the center of the Sun in solar radii ($R_\odot$). Columns (6) and (7): aspect ratio and half-angle of the CME, respectively.

CME front reconstruction


Post-CME blob reconstruction
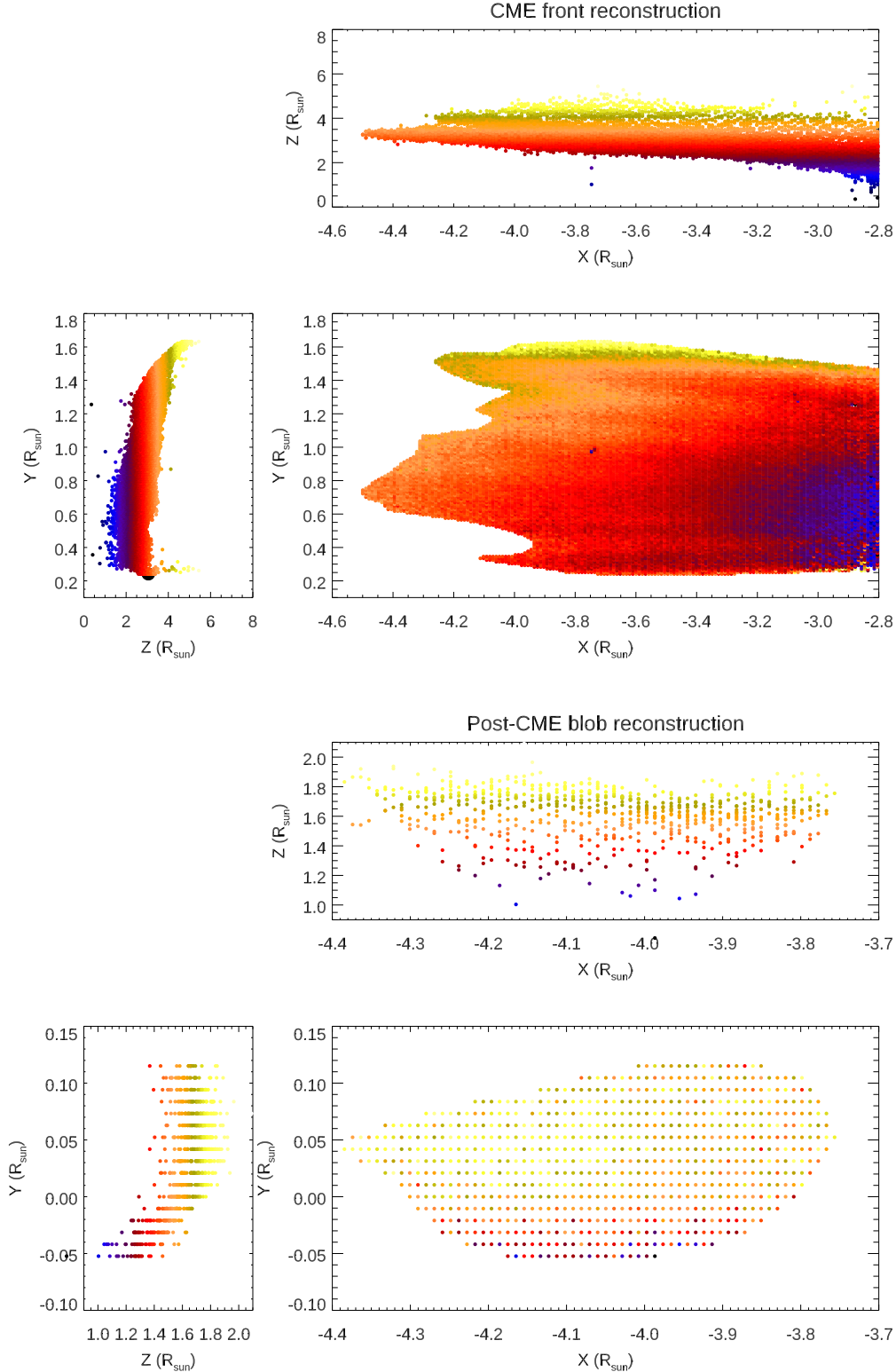
Fig. 13. 3D distribution of plasma-emitting elements as obtained from the polarization ratio technique applied to the VL Metis observations of the CME front (*top panels*) and the post-CME blob (*bottom panels*). Different colors correspond to different distances from the PoS (located at $Z = 0$) as given in the *left panels*.

on, the leading edge of the eruption is hardly visible in SWAP images. The derived longitude, latitude, and height are 85° west, 16° south and 1.447 $R_\odot$, respectively. This places the erupting prominence approximately 25° westward and 10° southward with respect to the main CME propagation direction as reconstructed by the VL coronagraphs. When we also consider the

value of the CME half-angle of about 30° as provided by the GCS reconstruction, this suggests that the prominence erupted from a region that was located on the disk very close to the possible location of the flanks of the expanding CME. This supports the possibility that the final prominence destabilization was related to the nearby CME expansion.
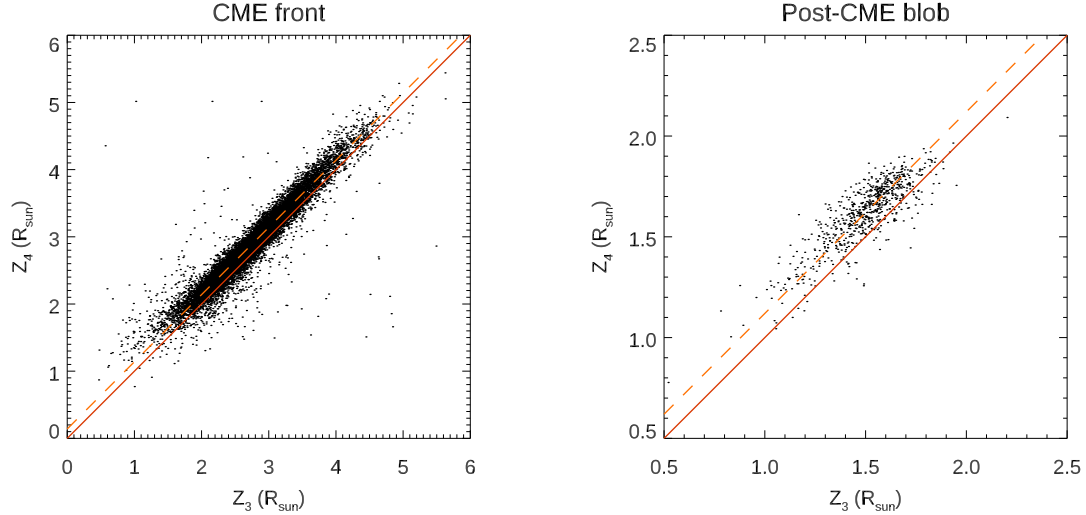
Fig. 14. Scatter plot comparisons between the distributions of LoS positions as obtained with the polarization ratio technique applied to the same Metis data points using four (Z_4) and three (Z_3) different orientations of the linear polarizer for the CME front (*left*) and the post-CME blob (*right*). The solid lines show the reference curve for $Z_4 = Z_3$, and the dashed lines show the best fit.

5. Reconstruction with polarization ratio

We also performed the 3D reconstructions with the polarization ratio technique (first described by Moran & Davila 2004) that has been applied by many different authors to reconstruct solar eruptions in 3D based on single viewpoint observations. This technique is particularly interesting for halo CMEs (e.g., Dolei et al. 2014; Lu et al. 2017), and results from this technique were compared and validated with multiple viewpoint observations (see, e.g., Mierla et al. 2010, 2011; Feng et al. 2013) and also with spectroscopic observations (Susino et al. 2014). Nevertheless, before Metis, all the coronagraphic space-based data so far were acquired in the VL and using only three different angular orientations of the linear polarizer, typically separated by 60° or 120°. This number of exposures may result in errors in the estimate of the pB and polarization angle, as investigated with magnetohydrodynamic (MHD) numerical simulations by Pagano et al. (2015) and more recently quantified by Inhester et al. (2021). These errors might be mitigated by acquiring a larger number of exposures.

With the Metis coronagraph, it is now possible for the first time to have sequences VL of coronagraphic images that were acquired with four different orientations of a linear polarizer, separated by ~45°(see Antonucci et al. 2020, for more details). Hence, the polarization ratio technique can be applied to pB and tB images for the first time that were derived from polarized sequences acquired with four different orientations of the linear polarizer. This is expected to reduce the uncertainties in the polarization measurement, hence smaller dispersion in the measurement of the LoS average position of the scattering plasma.

In order to quantify the advantages of using four polarimetric acquisitions instead of three, for the analysis performed here, we combined selected sequences of Metis VL polarized images in two different ways for the three and four polarizer orientations. Because Metis polarimetric observations are routinely performed using polarization angles $\delta_1 = 181.8°$, $\delta_2 = 49.1°$, $\delta_3 = 84.3°$, and $\delta_4 = 133.2°$, we neglected the fourth image of the selected sequences to simulate an acquisition obtained with only three polarizer orientations. The Stokes vector images, and in turn, the pB and tB images, were then derived from the three polarized images using the inverse of the theoretical Müller

matrix corresponding to the effective polarization angles δ_1, δ_2, and δ_3. Furthermore, to reliably compare the two cases, we also derived special pB and tB images from the full polarimetric sequence (i.e., also including the image corresponding to the δ_4 orientation) by using the theoretical Müller matrix instead of that measured during laboratory calibrations. This alternative approach is necessary because the laboratory Müller matrix has been derived from pixel-by-pixel measurements in order to account for inhomogeneities in the polarimetric response of Metis polarimeter. Therefore it cannot be used to derive the Stokes images from a subset of the four polarized images of a nominal sequence.

Starting from the resulting pB and tB images as obtained with four different orientations of the linear polarizer, we applied the polarization ratio technique to measure the LoS distribution of plasma-emitting elements located in the CME front and in the the post-CME blob. In particular, for the CME front, the technique was applied to the polarized sequence acquired by Metis on February 12 between 20:15 and 20:45 UT after subtracting the pre-CME sequence acquired on the same day between 13:15 and 13:45 UT. On the other hand, for the post-CME blob, the technique was applied to the polarized sequence acquired by Metis on February 13 between 08:15 and 08:45 UT after subtracting the previous sequence acquired on the same day between 07:15 and 07:45 UT. For comparison, the reconstructions were then also performed using the same images as obtained with only three different orientations of the linear polarizer.

The resulting 3D distributions are shown in Fig. 13 for the CME front (top three panels) and the post-CME blob (bottom three panels). The Cartesian coordinates are the same as those employed in Fig. 9. These measurements show that the CME front plasma was located at an average heliocentric distance of $h_{\rm front} = 3.65\,R_\odot$ and a distance from the PoS along the Metis LoS by $Z_{\rm front} = (2.87 \pm 0.57)\,R_\odot$, while the post-CME blob was at an average heliocentric distance of $h_{\rm blob} = 4.04\,R_\odot$, at an average distance from the PoS along the Metis LoS by $Z_{\rm blob} = (1.62 \pm 0.16)\,R_\odot$. In the Stonyhurst coordinates, the CME front therefore expanded at an average longitude $\theta_{\rm front} = 68°$ west, while the post-CME blob expanded at an average longitude $\theta_{\rm blob} = 85°$ west. These angles agree very well with values provided by the 3D reconstruction of the CME with the GCS model

and with the location of the erupting prominence derived with triangulation. This means that the post-CME blob, whose origin is unclear because it was observed only in the coronagraphic images and not in the EUV disk images, was almost aligned with the previous propagation of the erupting prominence. This suggests a clear association of the two events.

It is also interesting to compare the LoS coordinate distributions Z of the plasma-emitting points as obtained by Metis using images acquired with three (Z_3) or four (Z_4) different orientations of the linear polarizer. This interesting comparison, performed here for the very first time, is given by two scatter plots in Fig. 14 for the CME front (left panel) and the post-CME blob (right panel). Each panel shows the ideal reference curve for $Z_4 = Z_3$ (solid lines), and the best linear fitting curves (dashed lines). Fig. 14 shows that the LoS measurements of Z_3 as obtained only with three different orientations of the linear polarizer would be systematically underestimated by $0.14\,R_\odot$ and $0.12\,R_\odot$ on average for the CME front and the post-CME blob, respectively. These underestimates correspond to relative errors in the LoS positioning of 4.9% and 7.4%, respectively. This quantifies the improvement in the 3D reconstructions of CMEs based on the polarization ratio technique applied to the Metis data.

6. Summary and conclusions

We analyzed a complex sequence of three successive eruptive events that occurred on the Sun between 2021 February 12–13. During these days, the Sun released a slow and accelerating CME, followed by a nearby prominence eruption and a trailing plasma blob. The events have been observed not only by ground- and space-based instruments located along the Sun-Earth line, but also by the STEREO-A and Solar Orbiter spacecraft, located at separation angles with the Earth of 55.86° east and 161.6° east, respectively. The analysis presented here focused mostly on the data acquired by remote-sensing instruments on board Solar Orbiter, and was also supported by data acquired by other instruments; the main results are summarized here.

The combination of images acquired by different view points with triangulation (applied to FSI data) and GCS fitting technique (applied to Metis data) allowed us to reconstruct the 3D trajectory and source regions of the CME and the erupting prominence. The 3D location of the plasma blob was inferred with the polarization ratio technique. The CME originated in the western hemisphere (as seen from the Earth) and then propagated westward and northward. The following prominence erupted closer to the west limb (as seen from the Earth) and propagated northward. The subsequent blob followed approximately the same trajectory as the prominence.

These results once again confirm the importance of 3D reconstructions for measuring the real propagation speed and direction of solar eruptions, which were both different from what was determined from single view-point observations. This is important not only for space weather applications, but also for a physical interpretation of the observed events: in this case, the westward early CME propagation and its angular extension support a possible cause-effect association with the subsequent destabilization of the erupting prominence, making these two candidate sympathetic events. Moreover, the coalignment between the prominence and the following post-CME blob also suggests that the blob originating in the corona is likely due to magnetic reconnection that occurred in the corona after the transit of the prominence. All the events were also observed by the HI instrument, and despite the existing gap between the Metis

and HI instrument FoVs, the combined J-maps allowed us to clearly track the same features in the two instruments.

For the first time, a post-CME CS has been observed in the intermediate corona with a multichannel coronagraph in the VL and UV Ly-α. This radial feature appears as a classical intensity enhancement in the VL (because plasma is compressed in the CS), and an intensity depletion in the UV Ly-α (because the radial speeds and temperatures of plasma that propagates along the CS are higher), thus confirming previous UVCS observations of similar features in the H I Ly-α (Lin et al. 2005) and also in the Ly-β (Bemporad et al. 2006) lines. Also for the first time, the images acquired by the two Metis channels in VL and UV were combined to measure the plasma temperature gradient across the post-CME blob. The observed shift between the VL and UV blob location was explained here by assuming that the Ly-α emission is entirely collisional because of Doppler dimming. With this assumption (and by also assuming ionization equilibrium), the shift is explained by a radial temperature increase across the blob from 1.0×10^6 K in the ascending top part up to $\sim 1.55 \times 10^6$ K in the lower bottom part.

The polarization ratio technique applied to Metis images provides values for the 3D location of the CME that agree very well with 3D reconstructions obtained with other methods. Moreover, we quantified the improvement in the 3D reconstruction capabilities based on images acquired with four (instead of three) different polarization angles for the first time.

Before we conclude, it is interesting to discuss a possible explanation and the implications for the measured temperature gradient across the post-CME blob. Similar small-scale post-CME blobs are usually interpreted as a result of post-CME coronal rearrangement and magnetic reconnection (e.g., Lynch & Edmondson 2013), in particular, along the newly formed post-CME CS (see, e.g., Liu et al. 2009; Chae et al. 2017). These blobs are typically hardly observed in EUV disk images (Schanche et al. 2016), making it difficult to understand their origin, and are typically observed in post-CME CS (see, e.g., Ko et al. 2003; Vršnak et al. 2009). Recently, Lee et al. (2020) reported the identification of the same plasma blobs as observed by LASCO and also in ground-based images acquired by the K-Cor coronagraph, demonstrating that their formation is likely due to a tearing instability (Shibata & Tanuma 2001; Bárta et al. 2008) that occurs just above the tip of post-CME CS, leading to magnetic reconnection that in most cases accelerates these blobs upward. This also agrees with Reeves et al. (2019), who studied the formation of dense plasmoid-like structures that break up the post-CME CS by a tearing instability, whose plasma is heated predominantly by adiabatic compression rather than ohmic heating. This implies that the onset of the plasmoid instability increases the heating of the surrounding plasma by adiabatic compression as the inflow velocity increases.

These previous findings suggest that the temperature gradient reported here for the first time might be the result of post-eruption magnetic reconnection driven by tearing instability and occurring in the corona just below the plasma blob. This reconnection therefore causes the outward acceleration of the blob and additional heating of the plasma by adiabatic compression, resulting in the observed temperature gradient. Future observations of similar blobs by Metis will be helpful to confirm or refute this scenario.

References

Andretta, V., Bemporad, A., De Leo, Y., et al. 2021, A&A, 656, L14
Antonucci, E., Romoli, M., Andretta, V., et al. 2020, A&A, 642, A10
Auchère, F., Andretta, V., Antonucci, E., et al. 2020, A&A, 642, A6
Bárta, M., Vršnak, B., & Karlický, M. 2008, A&A, 477, 649
Bemporad, A., Poletto, G., Suess, S. T., et al. 2006, ApJ, 638, 1110
Bemporad, A., Poletto, G., Landini, F., & Romoli, M. 2008, Ann. Geophys., 26, 3017
Bemporad, A., Pagano, P., & Giordano, S. 2018, A&A, 619, A25
Berghmans, D., Hochedez, J. F., Defise, J. M., et al. 2006, Adv. Space Res., 38, 1807
Brueckner, G. E., Howard, R. A., Koomen, M. J., et al. 1995, Sol. Phys., 162, 357
Capuano, G. E., Dolei, S., Spadaro, D., et al. 2021, A&A, 652, A85
Chae, J., Cho, K., Kwon, R.-Y., & Lim, E.-K. 2017, ApJ, 841, 49
Chen, P. F. 2011, Liv. Rev. Sol. Phys., 8, 1
Dere, K. P., Del Zanna, G., Young, P. R., Landi, E., & Sutherland, R. S. 2019, ApJS, 241, 22
Dolei, S., Romano, P., Spadaro, D., & Ventura, R. 2014, A&A, 567, A9
Feng, L., Inhester, B., & Mierla, M. 2013, Sol. Phys., 282, 221
Frassati, F., Susino, R., Mancuso, S., & Bemporad, A. 2019, ApJ, 871, 212
Georgoulis, M. K., Nindos, A., & Zhang, H. 2019, Philos. Trans. R. Soc. London Ser. A, 377, 20180094
Giordano, S., Ciaravella, A., Raymond, J. C., Ko, Y. K., & Suleiman, R. 2013, J. Geophys. Res. (Space Phys.), 118, 967
Gopalswamy, N., Yashiro, S., Michalek, G., et al. 2009, Earth Moon Planets, 104, 295
Harvey, J. W., Bolding, J., Clark, R., et al. 2011, AAS Sol. Phys. Div. Meeting, 42, 17.45
Hochedez, J. F., Zhukov, A., Robbrecht, E., et al. 2005, Ann. Geophys., 23, 3149
Howard, R. A., Moses, J. D., Vourlidas, A., et al. 2008, Space Sci. Rev., 136, 67
Howard, R. A., Vourlidas, A., Colaninno, R. C., et al. 2020, A&A, 642, A13
Hudson, H. S., & Cliver, E. W. 2001, J. Geophys. Res., 106, 25199
Inhester, B. 2006, ArXiv e-prints [arXiv:astro-ph/0612649]
Inhester, B., Mierla, M., Shestov, S., & Zhukov, A. N. 2021, Sol. Phys., 296, 72
Jackson, B. V., Buffington, A., Hick, P. P., et al. 2004, Sol. Phys., 225, 177
Kilpua, E. K. J., Mierla, M., Zhukov, A. N., et al. 2014, Sol. Phys., 289, 3773
Ko, Y.-K., Raymond, J. C., Lin, J., et al. 2003, ApJ, 594, 1068
Kohl, J. L., Esser, R., Gardner, L. D., et al. 1995, Sol. Phys., 162, 313
Kohl, J. L., Noci, G., Cranmer, S. R., & Raymond, J. C. 2006, A&ARv, 13, 31
Kozarev, K. A., Raymond, J. C., Lobzin, V. V., & Hammer, M. 2015, ApJ, 799, 167
Lamy, P. L., Floyd, O., Boclet, B., et al. 2019, Space Sci. Rev., 215, 39
Lee, J.-O., Cho, K.-S., Lee, K.-S., et al. 2020, ApJ, 892, 129
Liewer, P. C., Hall, J. R., Howard, R. A., et al. 2011, J. Atmos. Sol.-Terr. Phys., 73, 1173
Lin, J., & Forbes, T. G. 2000, J. Geophys. Res., 105, 2375
Lin, J., Ko, Y. K., Sui, L., et al. 2005, ApJ, 622, 1251
Liu, W., & Ofman, L. 2014, Sol. Phys., 289, 3233
Liu, Y., Luhmann, J. G., Lin, R. P., et al. 2009, ApJ, 698, L51
Lu, L., Inhester, B., Feng, L., Liu, S., & Zhao, X. 2017, ApJ, 835, 188
Lugaz, N., Temmer, M., Wang, Y., & Farrugia, C. J. 2017, Sol. Phys., 292, 64
Lynch, B. J., & Edmondson, J. K. 2013, ApJ, 764, 87
Mancuso, S., Frassati, F., Bemporad, A., & Barghini, D. 2019, A&A, 624, L2
Mierla, M., Inhester, B., Antunes, A., et al. 2010, Ann. Geophys., 28, 203
Mierla, M., Chifu, I., Inhester, B., Rodriguez, L., & Zhukov, A. 2011, A&A, 530, L1
Moran, T. G., & Davila, J. M. 2004, Science, 305, 66
Müller, D., Nicula, B., Felix, S., et al. 2017, A&A, 606, A10
Müller, D., St. Cyr, O. C., Zouganelis, I., et al. 2020, A&A, 642, A1
Pagano, P., Bemporad, A., & Mackay, D. H. 2015, A&A, 582, A72
Palmerio, E., Nitta, N. V., Mulligan, T., et al. 2021, Front. Astron. Space Sci., 8, 695966
Pötzi, W., Veronig, A. M., Riegler, G., et al. 2015, Sol. Phys., 290, 951
Reeves, K. K., Török, T., Mikić, Z., Linker, J., & Murphy, N. A. 2019, ApJ, 887, 103
Robbrecht, E., & Berghmans, D. 2004, A&A, 425, 1097
Rochus, P., Auchère, F., Berghmans, D., et al. 2020, A&A, 642, A8
Romoli, M., Antonucci, E., Andretta, V., et al. 2021, A&A, 656, A32
Schanche, N. E., Reeves, K. K., & Webb, D. F. 2016, ApJ, 831, 47
Seaton, D. B., Berghmans, D., Nicula, B., et al. 2013, Sol. Phys., 286, 43
Shen, Y., & Liu, Y. 2012, ApJ, 752, L23
Shibata, K., & Tanuma, S. 2001, Earth Planets Space, 53, 473
Susino, R., & Bemporad, A. 2016, ApJ, 830, 58
Susino, R., Bemporad, A., & Dolei, S. 2014, ApJ, 790, 25
Temmer, M. 2021, Liv. Rev. Sol. Phys., 18, 4
Thernisien, A. 2011, ApJS, 194, 33
Thernisien, A., Vourlidas, A., & Howard, R. A. 2009, Sol. Phys., 256, 111
Thernisien, A., Vourlidas, A., & Howard, R. A. 2011, J. Atmos. Sol.-Terr. Phys., 73, 1156
Thompson, W. T. 2006, A&A, 449, 791
Thompson, W. T. 2009, Icarus, 200, 351
Thompson, W. T., & Reginald, N. L. 2008, Sol. Phys., 250, 443
Tripathi, D., Bothmer, V., & Cremades, H. 2004, A&A, 422, 337
Vásquez, A. M., van Ballegooijen, A. A., & Raymond, J. C. 2003, ApJ, 598, 1361
Vršnak, B., Poletto, G., Vujić, E., et al. 2009, A&A, 499, 905
Webb, D. F., & Howard, T. A. 2012, Liv. Rev. Sol. Phys., 9, 3
Wilson, M. L., Raymond, J. C., Lepri, S. T., et al. 2022, ApJ, 927, 27
Yashiro, S., Gopalswamy, N., Michalek, G., et al. 2004, J. Geophys. Res. (Space Phys.), 109, A07105
Zhukov, A. N. 2007, in Space Weather : Research Towards Applications in Europe 2nd European Space Weather Week (ESWW2), ed. J. Lilensten, Astrophys. Space Sci. Lib., 344, 5
Zhukov, A. N., & Auchère, F. 2004, A&A, 427, 705